Hindawi
Mathematical Problems in Engineering
Volume 2021, Article ID 8863335, 13 pages
https://doi.org/10.1155/2021/8863335

Research Article

Study on Quasi-Static Loading Protocols considering the Action Characteristics of Long-Period Ground Motions

Ke Yang, Bo Wang, Jiawei Zhang, Zhe Li, and Boquan Liu

School of Civil Engineering, Chang'an University, Xi'an 710064, China

Correspondence should be addressed to Bo Wang; chnwangbo@chd.edu.cn

Received 22 September 2020; Revised 11 December 2020; Accepted 24 December 2020; Published 8 February 2021

Academic Editor: José António Fonseca de Oliveira Correia

Due to abundant low-frequency components of long-period ground motions (LPGMs), long-period structures are susceptible to severe damage. The corresponding time-history displacement responses have significant "large-displacement" and "long-duration" characteristics. These action characteristics essentially reflect the different loading paths imposed on structures of LPGMs from ordinary ground motions (OGMs). Hence, revealing the influence mechanism of the action characteristics on the seismic performance of structural components is the key to investigating the influence of LPGMs on the whole structure. This paper presents a kind of quasi-static loading protocol considering the action characteristics of LPGMs. Firstly, nonlinear time-history analyses on structural systems subjected to 50 selected representative LPGMs were conducted. Inelastic cycles and corresponding amplitudes of time-history displacement responses under LPGMs were statistically analyzed through the rainflow method. Then, considering two of the most significant factors, structural period and target ductility, a prediction model of cycle number and cycle amplitude was obtained by regression. On this basis, the quasi-static loading protocol considering the action characteristics of LPGMs was developed. Proposed protocols can be directly applied to experimental investigations on the seismic performance for structural components under LPGMs.

1. Introduction

Long-period ground motions (LPGMs) refer to the far-field ground motions with predominant periods of 1~10 s or longer in general, whose cause is primarily related to the propagation path of seismic waves [1]. Existing researches [2–4] indicated that the time-history displacement responses of long-period structures under LPGMs have distinct characteristics of "large-displacement" and "long-duration." It essentially reflects different action paths imposed on structures of LPGMs from ordinary ground motions (OGMs). Plenty of researches [5–16] showed that the loading path has a remarkable influence on the strength and stiffness deterioration, deformation performance, energy dissipation capacity, and failure mechanism of structural components. Therefore, it can be considered that revealing the influence mechanism of the LPGMs action characteristics, "large-displacement" and "long-duration," on the seismic performance of structural components is the key to investigating the influence of LPGMs on the whole structure. Quasi-static loading protocols considering the action characteristics of LPGMs could provide a possibility for experimental investigation of seismic performance and failure mechanism for structural components subjected to LPGMs.

The loading history of ground motions imposed on structures can be regarded as a random loading process. The load time-history can be converted into a series of full or half cycles through a counting algorithm. Among the existing counting algorithms, the rainflow counting algorithm [17–20] is the most widely used one. It presents the consistency of the counting procedure with stress-strain characteristics of materials, the better consideration of cycle distribution of random loading, and reliable mechanical basis. In recent years, some quasi-static loading protocols [21–30] considering the action characteristics of practical ground motions have been developed based on the rainflow method. However, LPGMs were not considered in and the corresponding quasi-static loading protocols could not reflect the action characteristics of LPGMs.

Therefore, quasi-static loading protocols considering the action characteristics of LPGMs were proposed in this paper. Two types of structural components were taken as the engineering background: RC pier columns in the long-span bridge, which can be simplified as the single-degree-of-freedom (SDOF) system, and columns on the weak story of high-rise RC frame structure representing the multiple-degree-of-freedom (MDOF) system. Firstly, nonlinear time-history analyses on SDOF and MDOF systems subjected to 50 selected representative LPGMs were conducted. Inelastic cycles and corresponding amplitudes of time-history displacement responses were statistically analyzed through the rainflow method. Then, multiple influence factors of cycle number and cycle amplitude including the ground motion type, structural period, target ductility, strength reduction coefficient, and damping ratio were evaluated. Finally, considering two of the most significant factors, structural period and target ductility, a prediction model of cycle amplitude and cycle number was proposed by regression. On this basis, the quasi-static loading protocols for structural components in SDOF and MDOF systems under LPGMs were developed.

2. Nonlinear Time-History Analyses

2.1. Selection of Ground Motions. In this paper, the weighted average value of amplitude (β_1) between 2 s and 10 s on the spectrum curve of dynamic amplification coefficient [31] was used as the quantitative index to distinguish LPGMs from OGMs. 50 representative LPGMs from Chi-Chi earthquake, WenChuan earthquake, East Japan earthquake, and Tokachi earthquake were selected to conduct the nonlinear time-history analyses. 15 representative OGMs were also selected for the comparison.

2.2. Structural Model. RC pier column in the long-span bridge was simplified as the SDOF system, and high-rise RC frame structure was simplified as the MDOF system. The Bouc–Wen–Baber–Noori (BWBN) model [32–35] was adopted to simulate the hysteretic behavior of structural components. It comprehensively considers strength deterioration, stiffness deterioration, and the pinching effect. Hence, the cumulative structural damage caused by LPGMs could be well exhibited.

The motion equation of SDOF system is shown as follows:

$$m\ddot{u}(t) + c\dot{u}(t) + F(t) = f(t), \tag{1}$$

where m is the mass; c is the linear viscous damping coefficient; $\ddot{u}(t)$and $\dot{u}(t)$are the acceleration and velocity, respectively; $F(t)$ is the restoring force; $f(t)$ is the external excitation.

As shown in Figure 1, the restoring force of the BWBN model is provided by two parallel springs (linear and nonlinear). Correspondingly, $F(t)$ in equation (2) is the summation of linear restoring force $F_e(t)$ and nonlinear restoring force $F_h(t)$.

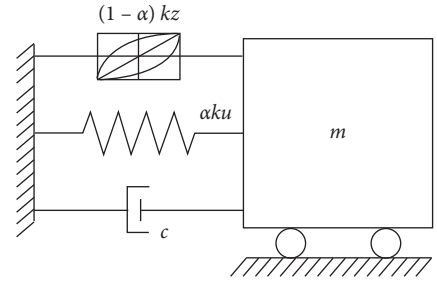

Figure 1: Bouc–Wen–Baber–Noori model.

$$F(t) = F_e(t) + F_h(t) = \alpha k u(t) + (1-\alpha) k z(t), \tag{2}$$

where α is the ratio of stiffness after yielding to stiffness before yielding; k is the initial linear elastic stiffness; $u(t)$ is the displacement; $z(t)$ is the hysteretic displacement, defined by the differential equation with initial condition $z(0) = 0$, as shown in the following equation:

$$\dot{z}(t) = h(z)\frac{A\dot{u} - \nu\left[\beta|\dot{u}||z|^{n-1}z + \gamma\dot{u}|z|^{n}\right]}{\eta}, \tag{3}$$

where A is the control parameter of hysteretic amplitude, $A = 1$; β, γ, and n are the shape parameters of hysteretic curves; υ and η are the strength and stiffness deterioration parameters, respectively.

$$\begin{aligned} \nu &= 1 + \delta_\nu \varepsilon, \\ \eta &= 1 + \delta_\eta \varepsilon, \end{aligned} \tag{4}$$

where δ_ν and δ_η are the strength and stiffness deterioration rates, respectively; ε is the cumulative hysteretic energy consumption.

$$\dot{\varepsilon} = (1-\alpha)\omega_0^2 z\dot{u}. \tag{5}$$

In equation (3), $h(z)$ is the function describing the pinching effect, as shown in following equation:

$$\begin{aligned} h(z) &= 1 - \zeta_1 \exp\left[-\left(\frac{z\,\mathrm{sign}(\dot{u}) - q z_{\max}}{\zeta_2}\right)^2\right], \\ \zeta_1 &= \zeta_s[1 - \exp(-p\varepsilon)], \\ \zeta_2 &= \left(\psi + \delta_\psi \varepsilon\right)(\lambda + \zeta_1), \\ z_{\max} &= \left[\frac{A}{\nu(\beta+\gamma)}\right]^{1/n}, \end{aligned} \tag{6}$$

where $\mathrm{sign}(\dot{u})$ is the symbolic function of velocity. When $\dot{u} > 0$, $\dot{u} = 0$, and $\dot{u} < 0$, $\mathrm{sign}(\dot{u})$ takes 1, 0, and -1, respectively. ζ_s, ψ, δ_ψ, λ, q, and p are the parameters of the pinching effect. Among them, ζ_s controls the total slippage; ψ controls the range of pinching; δ_ψ is the pinching rate; λ is the interaction coefficient between pinching severity and pinching rate; q controls the starting position of the pinch; p is the pinching slope.

The values of all parameters in the BWBN model adopted in this paper were obtained from Reference 35.

2.3. Nonlinear Time-History Analyses. Nonlinear time-history analyses on simplified structural models subjected to the selected ground motions were conducted through the iterative procedure shown in Figure 2. It should be pointed out that the results of the weak story with maximum drift ratio are required for the MDOF system. The ductility was expected as the control index in developed loading protocols. Therefore, the peak ground acceleration (PGA) of ground motion, as the iterative variable, was increased from 0 with a constant increment of 0.1 gal until the structural components reach the predetermined ductility (target ductility μ). The maximum ductility, which is defined as the ratio of the maximum displacement to the yield displacement ($\mu_{\max} = \delta_u/\delta_y$), was used as the target ductility [22].

3. Rainflow Cycle Counting

Rainflow method with an improved preliminary treatment was adopted in this paper. All cycles could be extracted by adopting rainflow cycle extraction only once. Through the improved rainflow method, the cycle counting procedure is simplified and a higher counting efficiency could be achieved. Figure 3 shows the rainflow cycle counting process taking a representative time-history displacement response as an example. Detailed counting procedures are as follows:

3.1. Convergence Processing. Convergence processing aimed to ensure the overall convergence of time-history displacement response. Reversing two segments separated by the point with the maximum absolute value on the curves and the convergence processing was accomplished.

3.2. Extrema Extraction. Extrema is the point whose displacement value on the time-history displacement response curves is larger (or less) than that of all two adjacent points. During the extraction, the extrema points were reserved, while the non-extrema points were discarded. The start and end points were directly reserved since they only have one adjacent point.

3.3. Cycle Counting. After convergence processing and extrema extraction, cycles could be extracted directly through the four-point rainflow cycle counting algorithm. The criterion of the cycle counting algorithm is shown in equations (7) and (8). A cycle could be counted when any of these criteria were satisfied, as shown in Figure 4. Corresponding cycle amplitude could be calculated by equation (9). At the end of the cycle counting, only three points were left forming the last cycle. An example of cycle counting is presented in Figure 5. The rainflow counting results of the representative time-history displacement response in ascending order of cycle amplitude is depicted in Figure 3.

$$D_i \le D_{i+2} \& D_{i+1} \le D_{i+3}, \quad i = 1, 2, \ldots, \tag{7}$$

$$D_i \ge D_{i+2} \& D_{i+1} \ge D_{i+3}, \quad i = 1, 2, \ldots, \tag{8}$$

$$D(n) = \frac{\left|D_{i+1} - D_{i+2}\right|}{2}, \quad i = 1, 2, \ldots, \tag{9}$$

where D_i is the displacement of the i-th point; $D(n)$ is the displacement amplitude of the n-th cycle.

4. Influence Factors of Cycle Number and Cycle Amplitude Distribution

Every inelastic cycle contributes to structural damage. The damage degree depends on the inelastic cycle number and cycle amplitude distribution, which are two important indicators for loading protocols. However, these two indicators could not be directly used for the comparison of loading protocols. Thus, the total inelastic cycle number N_{all} and the maximum cumulative displacement ductility $CDD_{\max}$ [21] were introduced to quantitatively describe the inelastic cycle number and cycle amplitude distribution.

The total inelastic cycle number N_{all} is the sum of all numbers of inelastic cycles. The maximum cumulative displacement ductility $CDD_{\max}$ is the sum of the cycle amplitudes corresponding to all inelastic cycles. Two loading protocols with the same N_{all} may have different cycle amplitude distributions, while those with the same $CDD_{\max}$ may have different inelastic cycle numbers and cycle amplitude distributions.

Multiple influence factors of cycle number and cycle amplitude distribution are evaluated as follows:

4.1. Ground Motion Type. Figures 6 and 7 present the total inelastic cycle number N_{all} and the maximum cumulative displacement ductility $CDD_{\max}$ of SDOF and MDOF systems with different periods under different types of ground motion, where the target ductility is 4; the strength reduction coefficient is 4; the damping ratio is 0.05. All the data are the average values.

It can be observed that the ground motion type had a significant influence on the total inelastic cycle number N_{all} and the maximum cumulative displacement ductility $CDD_{\max}$. The N_{all} and $CDD_{\max}$ under LPGMs were significantly larger than those under OGMs. This could be attributable to the "long-duration" action characteristics of LPGMs.

It also can be found that N_{all} and $CDD_{\max}$ of MDOF systems exhibited different trends from SDOF systems when the period was in the range of 4~6 s. The average values of N_{all} and $CDD_{\max}$ under LPGMs were visibly larger than those under OGMs, indicating that MDOF systems with a long period were prone to the influence of LPGMs.

4.2. Target Ductility and Structural Period. Figures 8 and 9 present the total inelastic cycle number N_{all} and the maximum cumulative displacement ductility $CDD_{\max}$ of SDOF

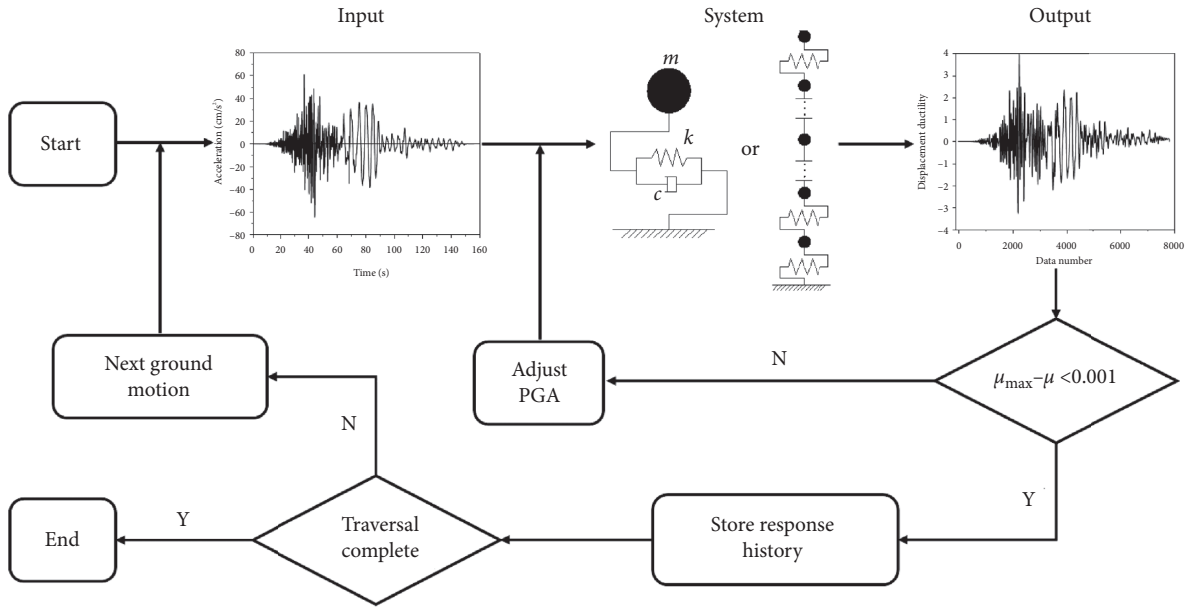

Figure 2: The iterative procedure of nonlinear time-history analyses.

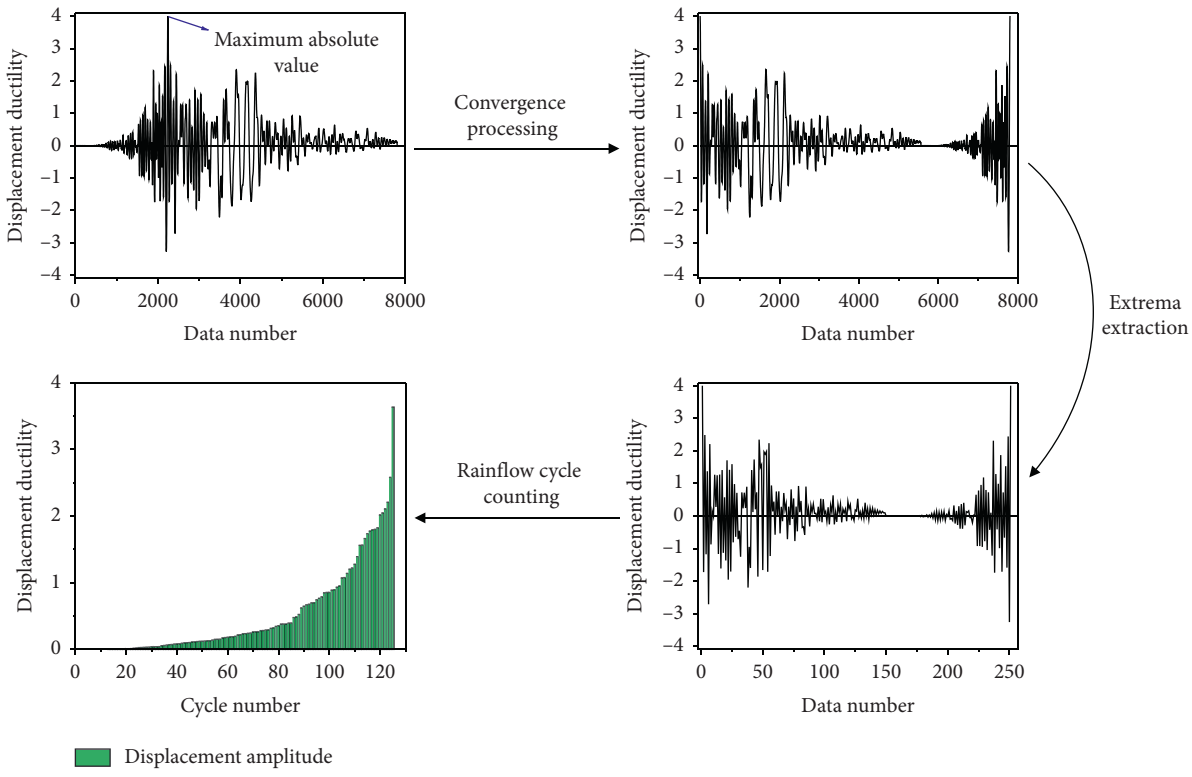

Figure 3: Rainflow cycle counting process.

and MDOF systems with different periods and target ductilities under LPGMs, where the strength reduction coefficient is 4; the damping ratio is 0.05; T is the structural period.

It can be observed that the target ductility and structural period had a remarkable influence on the total inelastic cycle number N_{all} and the maximum cumulative displacement ductility CDD_{max}. N_{all} and CDD_{max} increased with the increase in target ductility and the decrease in the structural period. N_{all} and CDD_{max} of SDOF and MDOF systems with different periods presented consistent trends as the target ductility increased. The reduction of N_{all} and CDD_{max} was significant when the period was less than 2 s, while it slowed down when the period was in the range of 2~6 s. CDD_{max} increased linearly as the target ductility increased, implying

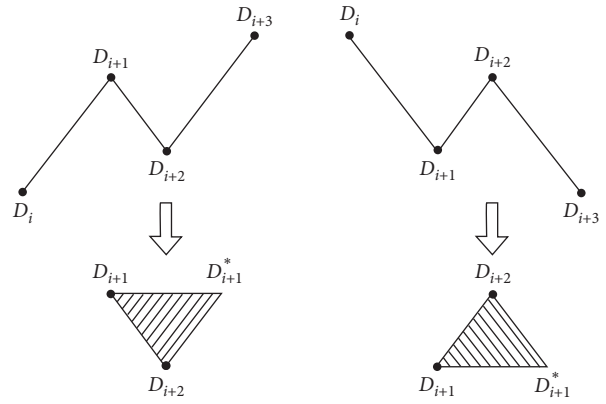

Figure 4: The criteria of cycle counting algorithm.

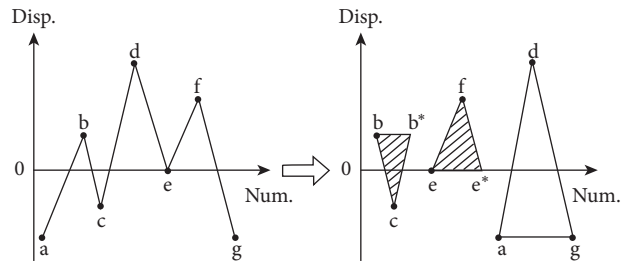

Figure 5: The cycle counting example.

that with the increase in target ductility, the structures suffered more serious damage at the later loading stage with larger cycle amplitude.

4.3. Strength Reduction Coefficient and Damping Ratio. Figures 10 and 11 present the total inelastic cycle number N_{all} and the maximum cumulative displacement ductility $CDD_{\max}$ of SDOF and MDOF systems with different strength reduction coefficients and damping ratios under LPGMs, where the target ductility is 4; the structural period is 2 s; ξ is the damping ratio.

It can be observed that SDOF and MDOF systems showed extremely distinctive characteristics of N_{all} and $CDD_{\max}$ varying the damping ratio. That might be attributable to the different calculation methods of structural damping in SDOF and MDOF systems. Linear viscous damping was adopted for the SDOF system, while the Rayleigh damping was adopted for the MDOF system.

For SDOF systems, N_{all} and $CDD_{\max}$ had the similar ascending trends increasing the strength reduction coefficient except when the strength reduction coefficient was 6. While compared with Figure 8, the growth of N_{all} and $CDD_{\max}$ caused by the increase in the strength reduction coefficient was less than that caused by the increase in target ductility and the decrease in the structural period. For MDOF systems, N_{all} and $CDD_{\max}$ had stable changing trends varying the strength reduction coefficient with the same damping ratio.

5. Prediction of Cycle Number and Cycle Amplitude

5.1. Double Exponential Prediction Model. From the above analyses, it can be found that the structural period and target ductility have the most significant influence on the cycle number and cycle amplitude distribution under a certain type of ground motion. Therefore, regression analyses on cycle numbers and cycle amplitudes of SDOF and MDOF systems with different periods and target ductilities under LPGMs were conducted. The double exponential function (equation (10)) was adopted to predict the cycle amplitude on the basis of the simple exponential function adopted in the existing researches [22, 30]. The boundary conditions are $D(1) = 1$ and $D(N_{\text{all}}) = \mu$.

$$D(N) = \frac{1}{e^{\alpha} - e^{\beta}}\left[\left(\mu - e^{\beta}\right)e^{\alpha(N-1)/\left(N_{\text{all}}-1\right)} - \left(\mu - e^{\alpha}\right)e^{\beta(N-1)/\left(N_{\text{all}}-1\right)}\right], \tag{10}$$

where $D(N)$ is the cycle amplitude corresponding to the N-th cycle; N is the cycle number, which equals 1, 2, 3, ... N_{all} in turn; α and β are the distribution parameters of the cycle amplitudes, which reflect the trend of cycle amplitude $D(N)$ with the change of cycle number N; μ is the target ductility.

5.1.1. The Total Inelastic Cycle Number: N_{all}. Quartic polynomial and quintic polynomial were utilized to fit the effect of target ductility (T) and structural period (μ) on the total inelastic cycle number N_{all}, respectively. For convenience, the fitting formula for N_{all} was exhibited in matrix form (equation (11)). All coefficients in quartic polynomial and quintic polynomial were integrated into a coefficient matrix C. C_S shown in equation (12) and C_M shown in equation (13) are the coefficient matrices obtained through the fitting process of N_{all} statistical results for the SDOF system and MDOF system, respectively. They can only be used in the cases studied in this paper. Corresponding variables related to T and μ are shown in equations (14) and (15), respectively.

$$N_{\text{all}}(T, \mu) = C. \times \left(L_T \times R_\mu\right), \tag{11}$$

$$C_S = \begin{bmatrix} -16.62 & -15.75 & 34.16 & -6.352 & 0.3829 \\ 43.47 & -32.81 & -10.94 & 1.914 & -0.1053 \\ -9.783 & 24.55 & 0.1291 & -0.02959 & 0 \\ -5.83 & -4.574 & 0.01212 & 0 & 0 \\ 1.982 & 0.2954 & 0 & 0 & 0 \\ -0.162 & 0 & 0 & 0 & 0 \end{bmatrix}, \tag{12}$$

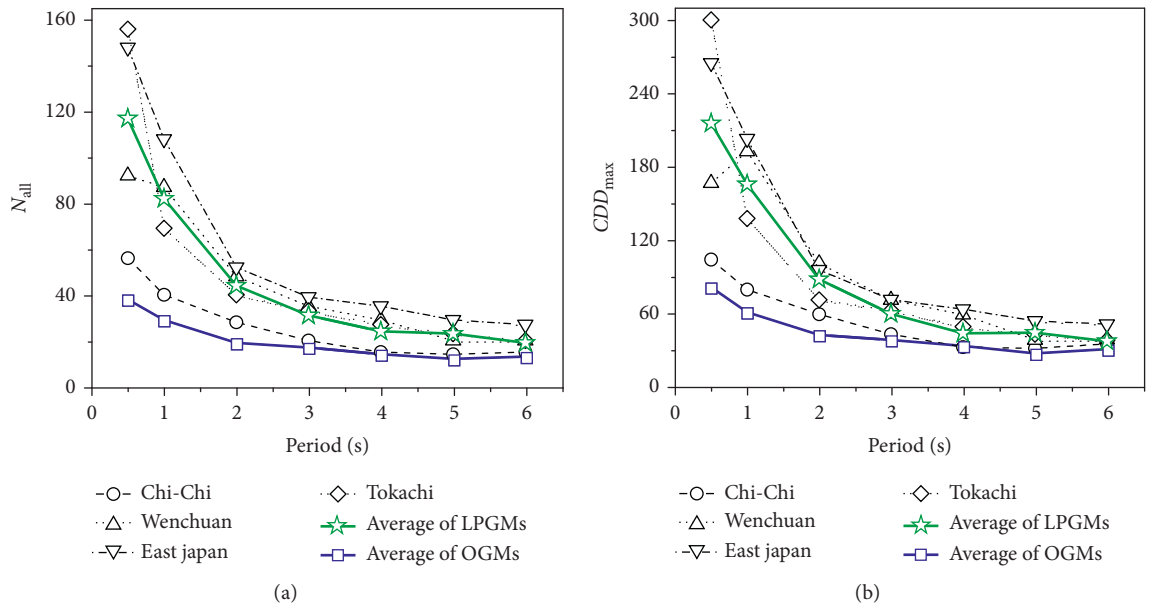

Figure 6: The influence of ground motion type on SDOF system. (a) The total inelastic cycle number. (b) The maximum cumulative displacement ductility.

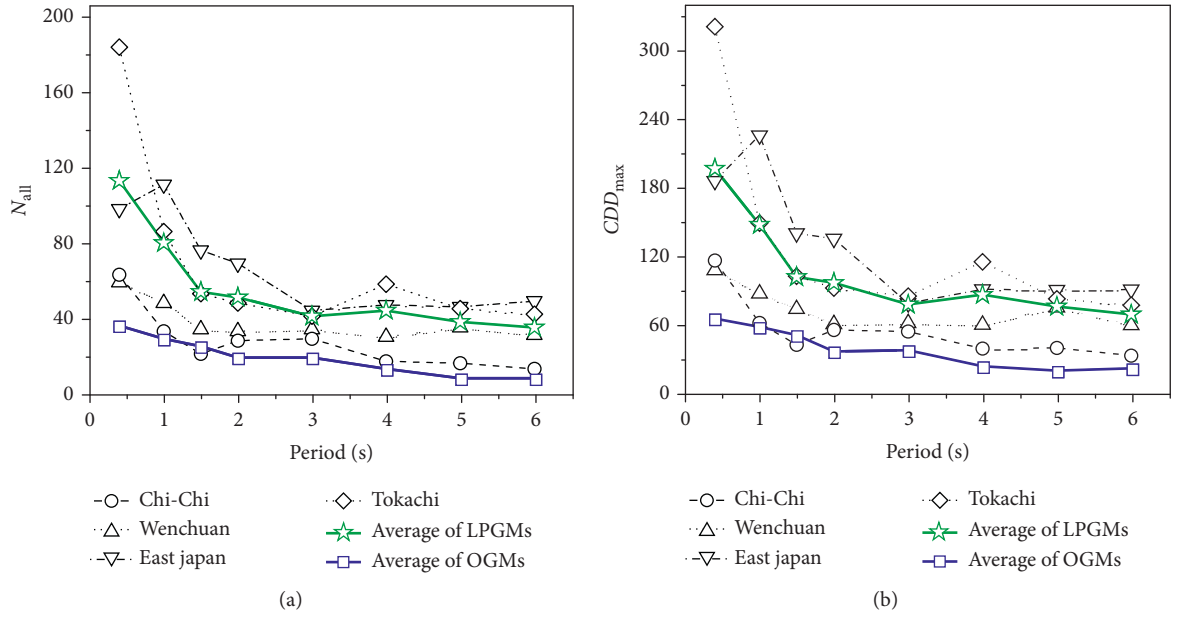

Figure 7: The influence of ground motion type on MDOF system. (a) The total inelastic cycle number. (b) The maximum cumulative displacement ductility.

$$C_M = \begin{bmatrix} -53.1600 & 26.4900 & 12.7200 & -2.1230 & 0.1035 \\ 52.5400 & -25.6100 & -5.8070 & 0.6520 & -0.0152 \\ -24.2300 & 14.8400 & 0.5777 & -0.0559 & 0 \\ 3.6100 & -2.8580 & 0.0078 & 0 & 0 \\ 0.0102 & 0.1725 & 0 & 0 & 0 \\ -0.0252 & 0 & 0 & 0 & 0 \end{bmatrix}, \tag{13}$$

$$L_T = \begin{bmatrix} 1 & T & T^2 & T^3 & T^4 & T^5 \end{bmatrix}^T, \tag{14}$$

$$R_\mu = \begin{bmatrix} 1 & \mu & \mu^2 & \mu^3 & \mu^4 \end{bmatrix}, \tag{15}$$

where C is the coefficient matrix, in which C_S is applied for SDOF systems and C_M is applied for MDOF systems; L_T is the column vector associated with the structural period T; R_μ is the row vector associated with the target ductility μ; symbol .× is the dot product operation of the matrix.

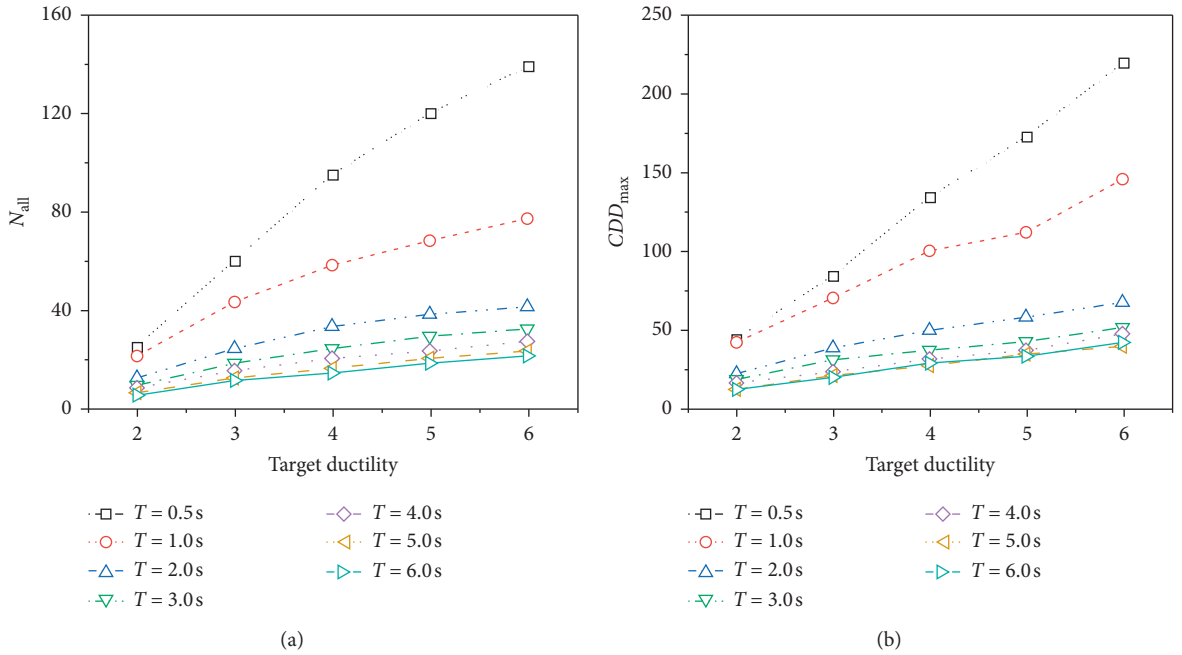

Figure 8: The influence of target ductility and structural period on SDOF system. (a) The total inelastic cycle number. (b) The maximum cumulative displacement ductility.

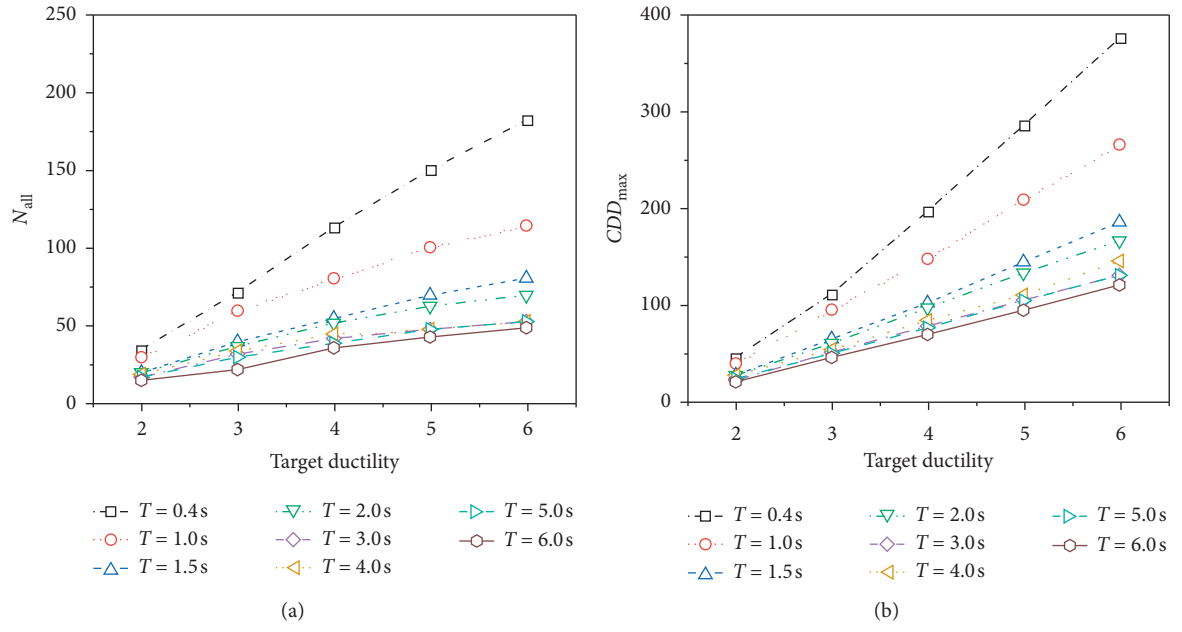

Figure 9: The influence of target ductility and structural period on MDOF system. (a) The total inelastic cycle number. (b) The maximum cumulative displacement ductility.

5.1.2. The Distribution Parameters of Cycle Amplitude: α and β. The cumulative distribution function (*CDF*) of cycle amplitudes [21] was introduced to describe the trend of cycle amplitude distribution with the change of cycle number. It can be derived by equation (16). Figure 12 presents the *CDF* of structures with different periods and target ductilities under LPGMs.

$$\text{CDF} = \frac{\sum N_i}{N_{\text{all}}}, \tag{16}$$

where ΣN_i is the number sum of cycles whose amplitude is less than or equal to the amplitude corresponding to the i-th cycle.

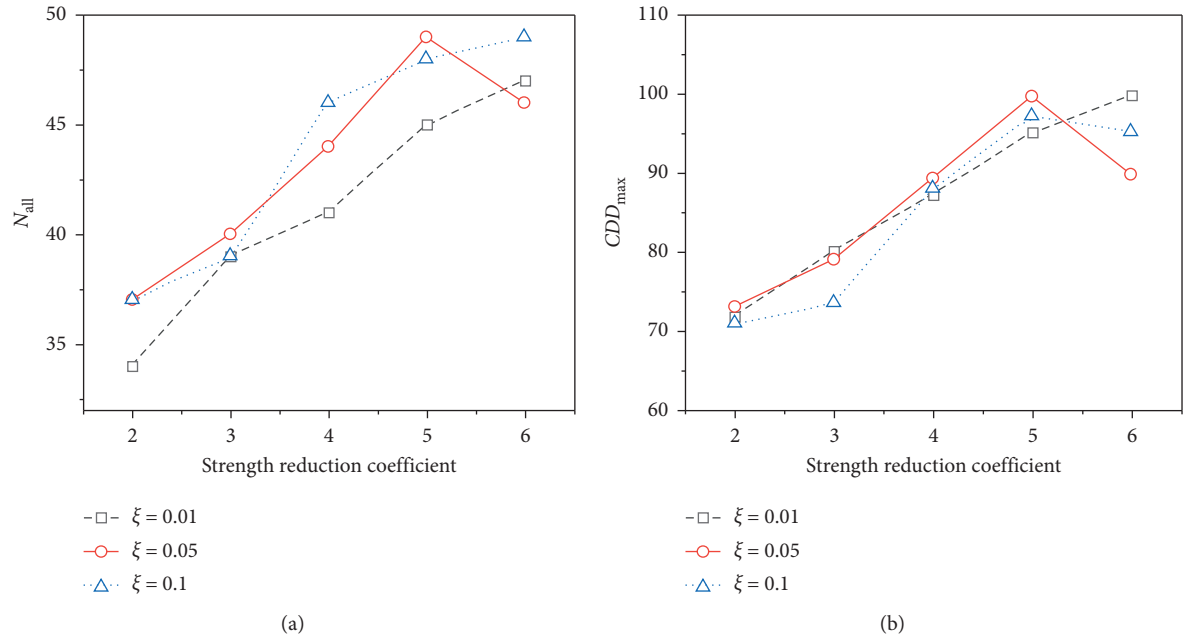

FIGURE 10: The influence of strength reduction coefficient and damping ratio on SDOF system. (a) The total inelastic cycle number. (b) The maximum cumulative displacement ductility.

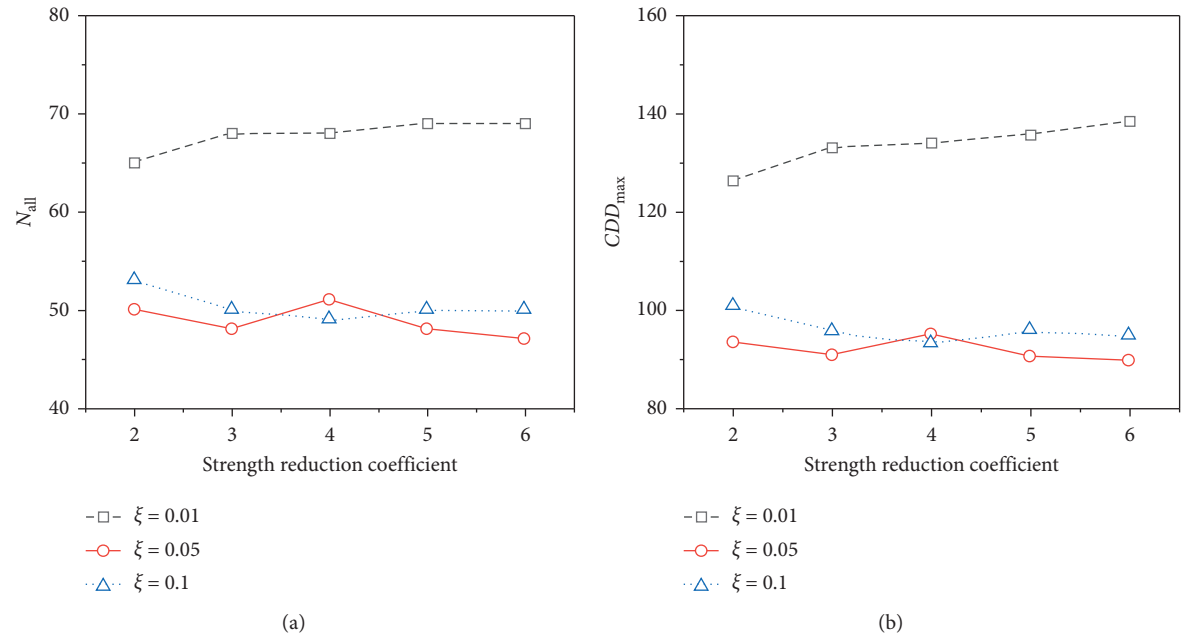

FIGURE 11: The influence of strength reduction coefficient and damping ratio on MDOF system. (a) The total inelastic cycle number. (b) The maximum cumulative displacement ductility.

It can be observed in Figures 12(a) and 12(b) that, with the same target ductility, *CDF* of structures with different periods were almost the same. They exhibited a greater agreement with each other as the target ductility increased. However, *CDF* of structures with the same period showed a high dependence on target ductility, as shown in Figure 12(c). For the same value of *CDF*, the larger the target ductility, the larger the corresponding cycle amplitude was. Meanwhile, for structures with the same period, as the target ductility increased, the growth rate of cycle amplitude increased, while the difference of cycle amplitudes under two adjacent target ductility levels decreased.

Accordingly, for structures with the same target ductility, the double exponential prediction model with the same α and β should be adopted. The values of α and β should be the optimal fitting results of equation (10) according to the

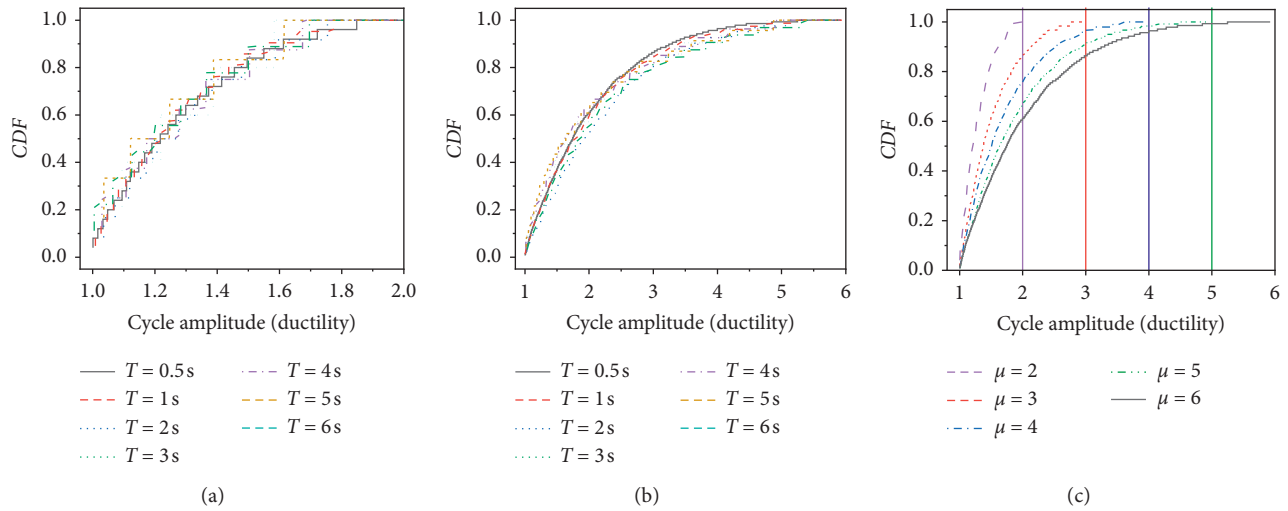

Figure 12: The *CDF* of structures with different periods and target ductilities. (a) $\mu = 2$, with different T. (b) $\mu = 6$, with different T. (c) $T = 0.5$ s with different μ.

statistical cycle numbers and cycle amplitudes. The calculated optimal fitting parameters α and β for SDOF and MDOF systems with different target ductilities are listed in Table 1.

Moreover, there was a small difference between cycle amplitudes of structures with two high adjacent target ductility levels. The growth rate of the cycle amplitude of structures with higher-level target ductility was larger. Therefore, when the value of ductility is a non-integer, the cycle number and cycle amplitude could be predicted by the parameter α and β under the closest integer high-level target ductility, as a conservative estimation value.

5.2. Prediction of Cycle Number and Cycle Amplitude. The cycle number and cycle amplitude of loading protocols considering the action characteristics of LPGMs could be directly predicted by the proposed double exponential prediction model, instead of conducting the nonlinear time-history analyses. The specific prediction steps are shown as follows:

Firstly, calculate the total inelastic cycle number N_{all} by equation (11) according to the structural period and target ductility. Then, obtain the values of distribution parameters of cycle amplitude α and β from Table 1 on the basis of the predetermined target ductility. Finally, the corresponding amplitudes of all cycles could be calculated by inputting the total inelastic cycle number N_{all} and distribution parameters α, β to equation (10).

5.3. Validation. In order to validate the accuracy and reliability of the proposed prediction model, three RC bridge pier columns (representing the SDOF system) and three RC frame structures (representing the MDOF system) were designed and analyzed. The top mass of all three pier columns is 500 t, the height is 5 m, 10 m, and 15 m, respectively. The uniaxial compressive strength of the concrete is 40 MPa. The elastic modulus of reinforced concrete is 31.62 GPa. The structural period is 1.14 s, 2.26 s, and 2.77 s, respectively. The equivalent stiffness of the columns is 15188.7 kN/m, 3864.7 kN/m, and 2572.6 kN/m, respectively. Three RC frame structures with 4, 8, and 12 stories [4] were designed according to the Chinese seismic design code [36]. The seismic precautionary intensity is 8-degree. The site condition is site-class 3. The structural fundamental period is 0.54 s, 1.17 s, and 2.18 s, respectively. For all systems, the damping ratio is 0.05 and the target ductility is 4.

The nonlinear time-history analyses and rainflow cycle counting were carried out first, obtaining the counting values of cycle numbers and cycle amplitudes. Then, the predicted values of cycle numbers and cycle amplitudes were obtained by the proposed prediction model. Figures 13–15 present the comparison of the counting value and predicted value in cycle number, cycle amplitude, and cumulative displacement ductility.

It can be observed that the predicted values of cycle numbers were in good agreement with the counting values. The predicted values of cycle amplitude basically coincided with counting values in the earlier stage, while those were slightly different from counting values in the later stage. This difference had a relatively small impact on the whole prediction model due to the large cycle amplitude in the later stage.

It also can be seen that the predicted values and counting values of cumulative displacement ductility were almost the same. This implied that, from the perspective of cumulative damage, the difference of cycle amplitude values in the later stage had almost no influence. It further validated the accuracy and reliability of the proposed double exponential prediction model.

6. Developed Quasi-Static Loading Protocols

Quasi-static loading protocols considering the action characteristics of LPGMs were developed based on the proposed double exponential prediction model. The

Table 1: Calculated distribution parameters of cycle amplitude a and β.

Structural system	Parameter	Target ductility μ				
		2	3	4	5	6
SDOF system	α	7.495	12.16	15.78	20.88	25.96
	β	0.4199	0.6847	0.8765	1.068	1.207
MDOF system	α	8.685	9.867	12.94	16.38	19.09
	β	0.4759	0.7014	0.9353	1.146	1.314

Note. The values in the table can only be used in the cases studied in this paper.

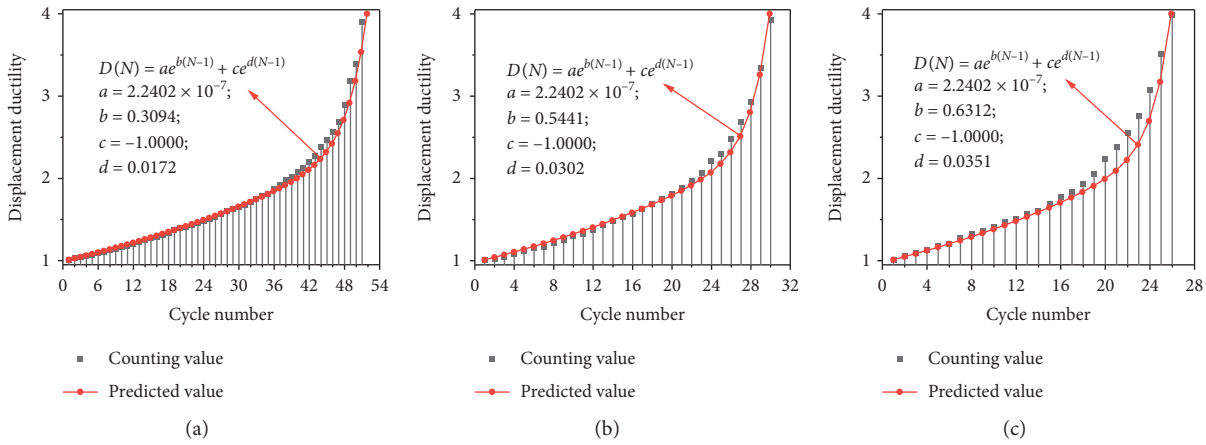

Figure 13: Validation of the cycle number and cycle amplitude for SDOF system. (a) $\mu = 4$; $T = 1.14$ s. (b) $\mu = 4$; $T = 2.26$ s. (c) $\mu = 4$; $T = 2.77$ s.

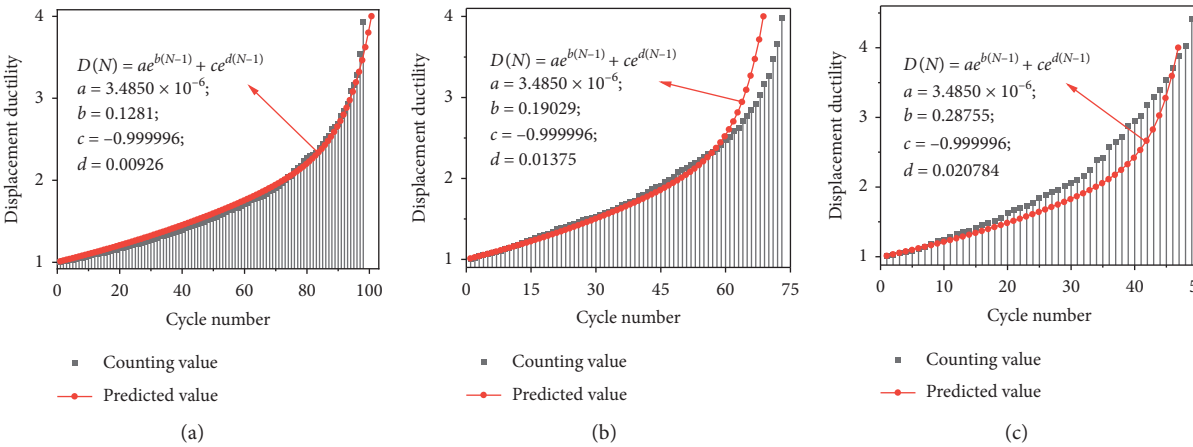

Figure 14: Validation of the cycle number and cycle amplitude for MDOF system. (a) $\mu = 4$; $T = 0.54$ s. (b) $\mu = 4$; $T = 1.17$ s. (c) $\mu = 4$; $T = 2.18$ s.

protocols consist of two stages: force-control loading stage and displacement-control loading stage. The RC pier column ($\mu = 4$, $T = 2.26$ s) and the column on weak story of the RC frame structure ($\mu = 4$, $T = 2.18$ s) were taken as examples. Developed quasi-static loading protocols are shown in Figure 16.

6.1. The First Loading Stage (Force-Control Loading Stage). When the cycle amplitude was less than the yield displacement δ_y, that is, before the yielding of structural components, there was almost no damage. Hence, loading protocols in different cases could adopt the same loading method in this stage. Force-control loading was employed in this paper. There are two cycles, as shown in Figure 16. The first cycle is applied with the amplitude of 0.75 F_y (F_y is the theoretical yield load of structural components). The second cycle is applied with the amplitude of F_y. The yielding of the column depends on the tension strain of longitudinal rebars on the control section. The lateral displacement of the horizontal actuator could be regarded as the yield displacement (δ_y) when the tension strain of longitudinal rebars on the control section reached the yield strain.

6.2. The Second Loading Stage (Displacement-Control Loading Stage). This stage aimed to reflect the influence of LPGMs action characteristics on structural components, which is the

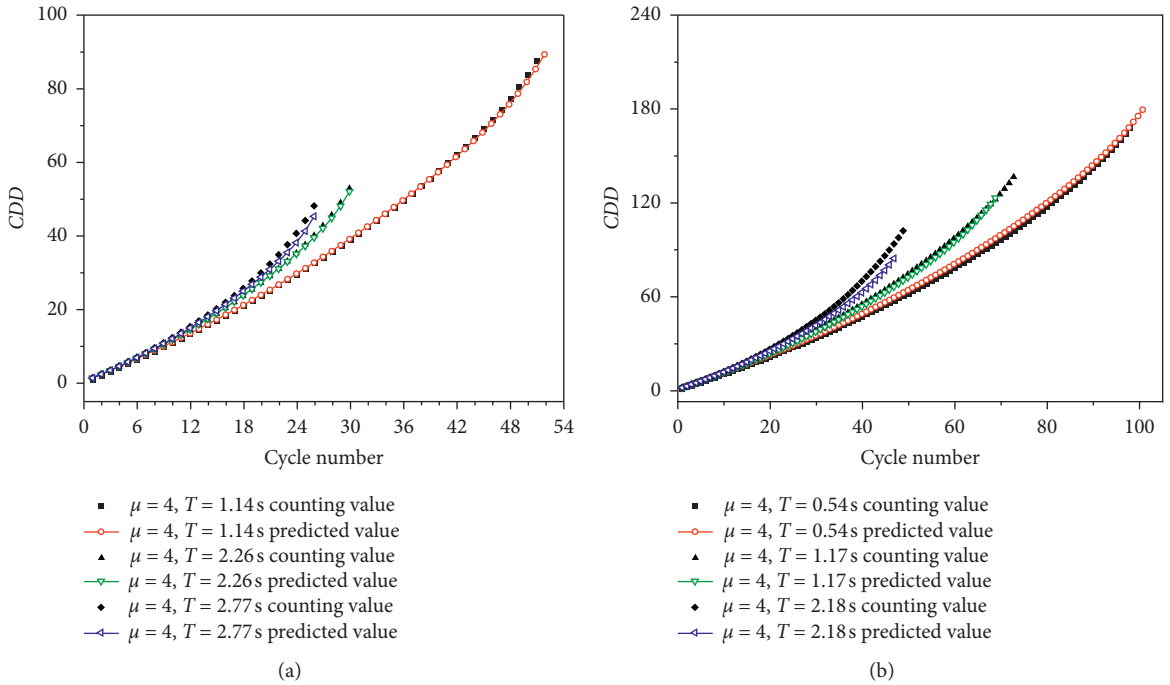

Figure 15: Validation of the cumulative displacement ductility. (a) SDOF system. (b) MDOF system.

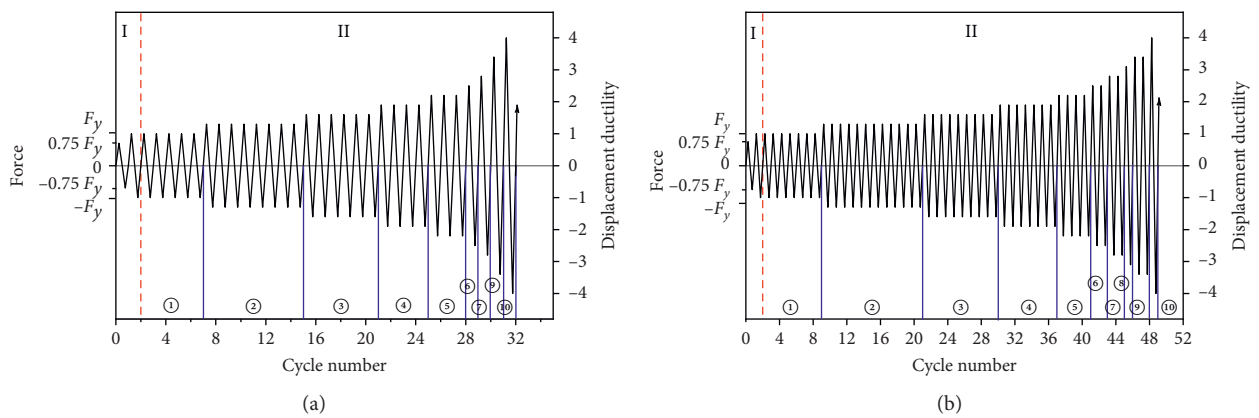

Figure 16: Developed quasi-static loading protocols for SDOF and MDOF systems under LPGMs. (a) SDOF system ($T = 2.26$ s). (b) MDOF system ($T = 2.18$ s).

critical part of the developed loading protocols. Cycle numbers and cycle amplitudes in this stage were predicted by the proposed prediction model, as shown in Figures 13(b) and 14(c).

In order to regularize the loading protocols, it is necessary to grade the predicted cycle amplitude and recount corresponding cycle numbers. The target displacement amplitude, i.e., the target ductility (μ) multiplied the yield displacement (δ_y), was divided to 10 grades with an approximately equal interval. The cycle numbers corresponding to the graded cycle amplitudes were recounted based on the predicted results, as shown in Table 2.

It can be found in Table 2 that, in the second loading stage, RC columns may be at the state of long-term damage accumulation instead of failure. In this case, the conventional quasi-static loading protocols with a monotone increase of cycle amplitude should be applied after the second loading stage until the failure occurred. Thereby, damage accumulation and residual bearing capacity of structural components considering the action characteristics of LPGMs could be comprehensively analyzed through the quasi-static tests.

The developed quasi-static protocol (Figure 16(b)) was applied on an RC column, and the structural response was compared with that under the time-history response subjected to an LPGM record, in order to verify the accuracy and efficiency of the developed quasi-static loading protocol. Figure 17 shows the time-history displacement response of the weak story in the 12-story RC frame structure ($T = 2.18$ s) subjected to an

Table 2: The graded cycle amplitudes and corresponding cycle numbers.

Grade		①	②	③	④	⑤	⑥	⑦	⑧	⑨	⑩
Graded cycle amplitude ($\times\delta_y$)		1	1.3	1.6	1.9	2.2	2.5	2.8	3.1	3.4	4
Cycle number	SDOF system	5	8	6	4	3	1	1	0	1	1
	MDOF system	7	12	9	7	4	2	2	1	2	1

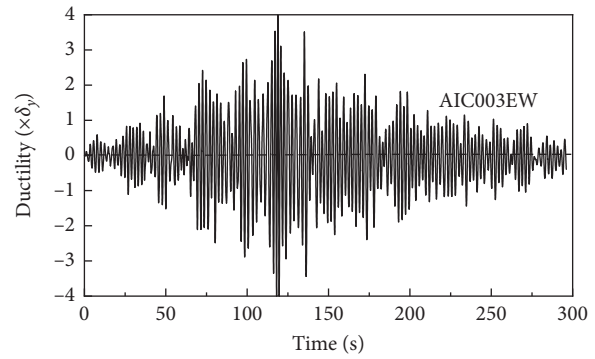

Figure 17: Time-history displacement response subjected to AIC003EW.

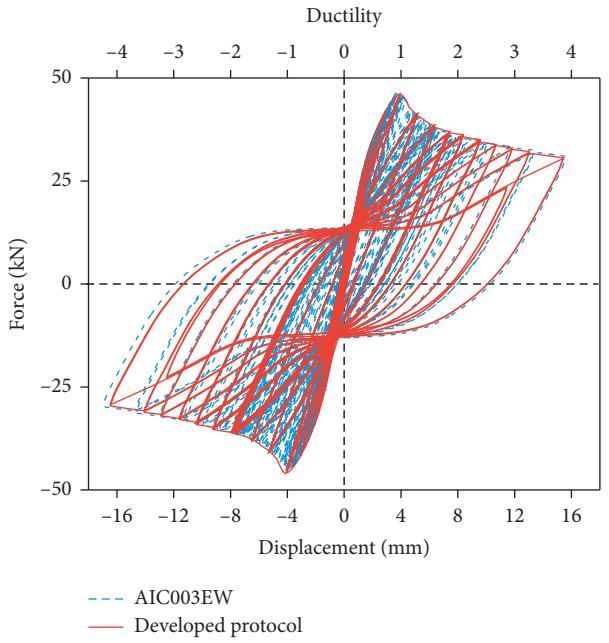

Figure 18: Comparison of the structural response.

LPGM record (AIC003EW from East Japan Earthquake). Comparison of the structural response is presented in Figure 18.

It can be found that the structural response under the developed protocol showed a good agreement with that under the seismic time-history response. This indicated that the proposed quasi-static protocols are reasonable to consider and reflect the seismic response characteristics of structural systems subjected to LPGMs.

In fact, the target ductility of the specific structural component is difficult to directly determine in practical application. For structural components in the MDOF system, the inter-story drift ratio could be used as the control index instead of ductility. That is, the target ductility could be determined by the target drift ratio, as shown in the following equation:

$$\mu = \frac{\theta h}{\delta_y}, \tag{17}$$

where θ is the target drift ratio; h is the storey height; δ_y is the yield displacement, which can be obtained through conventional quasi-static tests.

In this case, developed quasi-static loading protocols could be applied to experimental investigations of structural components in MDOF systems.

7. Conclusions

Quasi-static loading protocols considering the action characteristics of LPGMs were developed in this paper. They were developed by statistical and regression analysis based on the results of nonlinear time-history analyses considering LPGMs imposed on different structural systems with various periods and target ductilities. The structural response under developed protocols was in accordance with that under the time-history response subjected to LPGMs. Proposed loading protocols can be directly applied to the experimental study on the seismic performance of RC pier columns and columns on the weak story of the high-rise RC frame structure subjected to LPGMs. It provides a new method investigating the influence of LPGMs on the seismic performance of structural components.

Data Availability

The data supporting the findings of this study are available from the corresponding author upon request.

Conflicts of Interest

The authors declare that there are no conflicts of interest regarding the publication of this paper.

Acknowledgments

This work was supported by the National Natural Science Foundation of China (NSFC; Grant Nos. 51708037 and 51978076) and the Fundamental Research Funds for the Central Universities (Grant No. 300102280202).

References

[1] K. Koketsu and H. Miyake, "A seismological overview of long-period ground motion," *Journal of Seismology*, vol. 12, no. 2, pp. 133–143, 2008.

[2] Y. L. Chung, T. Nagae, T. Hitaka, and M. Nakashima, "Seismic resistance capacity of high-rise buildings subjected to long-period ground motions: E-defense shaking table test," *Journal of Structural Engineering*, vol. 136, no. 6, pp. 637–644, 2010.

[3] I. Takewaki, S. Murakami, K. Fujita, S. Yoshitomi, and M. Tsuji, "The 2011 off the pacific coast of Tohoku earthquake and response of high-rise buildings under long-period ground motions," *Soil Dynamics and Earthquake Engineering*, vol. 31, no. 11, pp. 1511–1528, 2011.

[4] B. Wang, *Study on Dynamic Behavior and Design Method of High-Rise Structures under Multi-type Long Period Ground Motions*, Xi'an University of Architecture and Technology, Xi'an, China, 2013, in Chinese.

[5] K. Kawashima and T. Koyama, "Effect of number of loading cycles on dynamic characteristics of reinforced concrete bridge pier columns," *Structural Engineering/Earthquake Engineering*, vol. 5, no. 1, pp. 205–213, 1988.

[6] S. Pujol, M. A. Sozen, and J. A. Ramirez, "Displacement history effects on drift capacity of reinforced concrete columns," *ACI Structural Journal*, vol. 103, no. 2, pp. 253–262, 2006.

[7] B. Acun and H. Sucuoğlu, "The effect of displacement history on the performance of concrete columns in flexure," *Advances in Performance-Based Earthquake Engineering*, vol. 13, pp. 373–382, 2010.

[8] J. C. Goodnight, M. J. Kowalsky, and J. M. Nau, "Effect of load history on performance limit states of circular bridge columns," *Journal of Bridge Engineering*, vol. 18, no. 12, pp. 1383–1396, 2013.

[9] J. C. Goodnight, M. J. Kowalsky, and J. M. Nau, "Strain limit states for circular RC bridge columns," *Earthquake Spectra*, vol. 32, no. 3, pp. 1627–1652, 2016.

[10] J. C. Goodnight, M. J. Kowalsky, and J. M. Nau, "Modified plastic-hinge method for circular RC bridge columns," *Journal of Structural Engineering*, vol. 142, no. 11, 2016.

[11] Y. H. Feng, M. J. Kowalsky, and J. M. Nau, "Effect of seismic load history on deformation limit states for longitudinal bar buckling in RC circular columns," *Journal of Structural Engineering*, vol. 141, no. 8, 2015.

[12] M. J. Kowalsky, "Deformation limit states for circular reinforced concrete bridge columns," *Journal of Structural Engineering*, vol. 126, no. 8, pp. 869–878, 2000.

[13] N. E. Cook and K. H. Gerstle, "Load history effects on structural members," *Journal of Structural Engineering*, vol. 111, no. 3, pp. 628–640, 1985.

[14] P. Lukkunaprasit and J. Thepmangkorn, "Load history effect on cyclic behavior of reinforced concrete tied columns," *Journal of Structural Engineering*, vol. 130, no. 10, pp. 1629–1633, 2004.

[15] S. Ergun and A. Demir, "Effect of hysteretic models on seismic behavior of existing RC structures," *Journal of Performance of Constructed Facilities*, vol. 29, no. 6, 2014.

[16] D. V. Syntzirma, S. J. Pantazopoulou, and M. Aschheim, "Load-history effects on deformation capacity of flexural members limited by bar buckling," *Journal of Structural Engineering*, vol. 136, no. 1, pp. 1–11, 2010.

[17] S. D. Dowing and D. F. Socie, "Simple rainflow counting algorithms," *International Journal of Fatigue*, vol. 4, no. 1, pp. 31–40, 1982.

[18] American Society for Testing and Materials (ASTM), *Standard Practices for Cycle-Counting in Fatigue Analysis, ASTM Standard E1049-85*, ASTM International, West Conshohocken, PA, USA, 2011.

[19] C. O. Viana, H. Carvalho, J. Correia et al., "Fatigue assessment based on hot-spot stresses obtained from the global dynamic analysis and local static sub-model," *International Journal of Structural Integrity*, 2019.

[20] C. S. Alencar, A. M. P. De Jesus, and R. Calcada, "Efficient computational approach for fatigue assessment of riveted connections," *Journal of Constructional Steel Research*, vol. 153, pp. 1–18, 2019.

[21] Y. C. Ou, J. W. Song, P. H. Wang, L. Adidharma, K. C. Chang, and G. C. Lee, "Ground motion duration effects on hysteretic behavior of reinforced concrete bridge columns," *Journal of Structural Engineering*, vol. 140, no. 3, pp. 36–49, 2014.

[22] R. Bazaez and P. Dusicka, "Cyclic loading for RC bridge columns considering subduction megathrust earthquake," *Journal of Bridge Engineering*, vol. 21, no. 5, 2016.

[23] B. Shafei and F. Zareian, "Development of a quasi-static loading protocol for displacement-sensitive nonstructural building components," in *Proceedings of the 14th World Conference on Earthquake Engineering WCEE*, Beijing, China, October 2008.

[24] H. Krawinkler, F. Parisi, L. Ibarra, A. Ayoub, and R. Medina, *Development of a Testing Protocol for Woodframe Structures*, Stanford University, Stanford, CA, USA, 2001.

[25] P. W. Richards and C.-M. Uang, "Testing protocol for short links in eccentrically braced frames," *Journal of Structural Engineering*, vol. 132, no. 8, pp. 1183–1191, 2006.

[26] Federal Emergency Management Agency (FEMA), *Interim Testing Protocols for Determining the Seismic Performance Characteristics of Structural and Nonstructural Components*, Vol. 461, Federal Emergency Management Agency (FEMA), Washington, DC, USA, 2007.

[27] R. Retamales, G. Mosqueda, A. Filiatrault, and A. Reinhorn, "Testing protocol for experimental seismic qualification of distributed nonstructural systems," *Earthquake Spectra*, vol. 27, no. 3, pp. 835–856, 2011.

[28] T. C. Hutchinson, J. Zhang, and C. Eva, "Development of a drift protocol for seismic performance evaluation considering a damage index concept," *Earthquake Spectra*, vol. 27, no. 4, pp. 1049–1076, 2011.

[29] T. C. Hutchinson and R. L. Wood, "Cyclic load protocol for anchored nonstructural components and systems," *Earthquake Spectra*, vol. 29, no. 3, pp. 817–842, 2013.

[30] P. E. Mergos and K. Beyer, "Loading protocols for European regions of low to moderate seismicity," *Bulletin of Earthquake Engineering*, vol. 12, no. 6, pp. 2507–2530, 2014.

[31] X. H. Li, W. K. Wang, D. Wu, X. L. Xu, Z. J. Li, and Y. R. Li, "The bounded method and characteristics analysis for long-period ground motions," *Journal of Vibration Engineering*, vol. 27, no. 5, pp. 685–692, 2014, in Chinese.

[32] K. Goda, H. P. Hong, and C. S. Lee, "Probabilistic characteristics of seismic ductility demand of SDOF systems with Bouc-Wen hysteretic behavior," *Journal of Earthquake Engineering*, vol. 13, no. 5, pp. 600–622, 2009.

[33] P. Sengupta and B. Li, "Modified Bouc-Wen model for hysteresis behavior of RC beam-column joints with limited transverse reinforcement," *Engineering Structures*, vol. 46, pp. 392–406, 2013.

[34] P. Sengupta and B. Li, "Hysteresis modeling of reinforced concrete structures: state of the art," *ACI Structural Journal*, vol. 114, no. 1, pp. 25–38, 2017.

[35] B. Yu and C. L. Ning, *Inelastic Seismic Dynamic Response Analysis and Parameter Identification for Engineering Structures*, Science Press, Beijing, China, 2016, in Chinese.

[36] Ministry of Construction of the People's Republic of China, *Code for Seismic Design of Buildings (GB50011-2010)*, China Architecture and Building Press, Beijing, China, 2016, in Chinese.